



HAL
open science

Multipacting mitigation by atomic layer deposition: The case study of titanium nitride

Y Kalboussi, Sarah Dadouch, B Delatte, F Miserque, D Dragoë, F Eozenou, M Baudrier, S Tusseau-Nenez, Y Zheng, L Maurice, et al.

► To cite this version:

Y Kalboussi, Sarah Dadouch, B Delatte, F Miserque, D Dragoë, et al.. Multipacting mitigation by atomic layer deposition: The case study of titanium nitride. *Journal of Applied Physics*, 2024, 136, pp.085306. 10.1063/5.0221943 . hal-04879943

HAL Id: hal-04879943

<https://hal.science/hal-04879943v1>

Submitted on 10 Jan 2025

HAL is a multi-disciplinary open access archive for the deposit and dissemination of scientific research documents, whether they are published or not. The documents may come from teaching and research institutions in France or abroad, or from public or private research centers.








L'archive ouverte pluridisciplinaire **HAL**, est destinée au dépôt et à la diffusion de documents scientifiques de niveau recherche, publiés ou non, émanant des établissements d'enseignement et de recherche français ou étrangers, des laboratoires publics ou privés.



Distributed under a Creative Commons Attribution - NonCommercial - NoDerivatives 4.0 International License

RESEARCH ARTICLE | AUGUST 29 2024

Multipacting mitigation by atomic layer deposition: The case study of titanium nitride

Y. Kalboussi ; S. Dadouch; B. Delatte; F. Miserque; D. Dragoe ; F. Eozenou ; M. Baudrier; S. Tusseau-Nenez; Y. Zheng; L. Maurice; E. Cenni; Q. Bertrand; P. Sahuquet; E. Fayette; G. Jullien ; C. Inguibert ; M. Belhaj ; T. Proslie 



J. Appl. Phys. 136, 085306 (2024)

<https://doi.org/10.1063/5.0221943>



Articles You May Be Interested In

Multipactor threshold sensitivity to total electron emission yield in small gap waveguide structure and TEEY models accuracy

Phys. Plasmas (December 2016)

Secondary electron emission characteristics of nanostructured silver surfaces

J. Appl. Phys. (October 2017)

Atypical secondary electron emission yield curves of very thin SiO₂ layers: Experiments and modeling

J. Appl. Phys. (October 2021)



Journal of Applied Physics

Special Topics Open for Submissions

[Learn More](#)

Multipacting mitigation by atomic layer deposition: The case study of titanium nitride

Cite as: J. Appl. Phys. 136, 085306 (2024); doi: 10.1063/5.0221943

Submitted: 4 June 2024 · Accepted: 29 July 2024 ·

Published Online: 29 August 2024



Y. Kalboussi,^{1,a)} S. Dadouch,² B. Delatte,¹ F. Miserque,³ D. Dragoe,⁴ F. Eozenou,¹ M. Baudrier,¹ S. Tusseau-Nenez,⁵ Y. Zheng,⁶ L. Maurice,¹ E. Cenni,¹ Q. Bertrand,¹ P. Sahuquet,¹ E. Fayette,¹ G. Jullien,¹ C. Inguibert,² M. Belhaj,² and T. Proslie^{1,a)}

AFFILIATIONS

¹Département des Accélérateurs, de la Cryogénie et du Magnétisme, Université Paris-Saclay, CEA, 91191 Gif-sur-Yvette, France

²Département Physique, Instrumentation, Environnement, Espace, ONERA, 31055 Toulouse, France

³Service de Recherche sur la Corrosion et le Comportement des Matériaux, Université Paris-Saclay, 91191 Gif sur Yvette, France

⁴Institut de Chimie Moléculaire et des Matériaux d'Orsay, Université Paris-Saclay, 91400 Orsay, France

⁵Laboratoire de Physique de la Matière Condensée, CNRS-Ecole polytechnique, 91120 Palaiseau, UMR 7643, France

⁶Institut des NanoSciences de Paris, CNRS-Sorbonne Université, 75005 Paris, UMR7588, France

^{a)}Authors to whom correspondence should be addressed: yasmine.kalboussi@cea.fr and thomas.proslie@cea.fr

ABSTRACT

This study investigates the use of atomic layer deposition (ALD) to mitigate multipacting phenomena inside superconducting radio frequency cavities used in particle accelerators while preserving high quality factors in the 10^{10} range. The unique ALD capability to control the film thickness down to the atomic level on arbitrary complex shape objects enables the fine-tuning of TiN film resistivity and total electron emission yield (TEEY) from coupons to devices. This level of control allows us to adequately choose a TiN film thickness that provides both high resistivity to prevent Ohmic losses and a low TEEY to mitigate multipacting for the application of interest. The methodology presented in this work can be scaled to other domains and devices subject to RF fields in vacuum and sensitive to multipacting or electron discharge processes with their own requirements in resistivities and TEEY values.

© 2024 Author(s). All article content, except where otherwise noted, is licensed under a Creative Commons Attribution-NonCommercial-NoDeriv 4.0 International (CC BY-NC-ND) license (<https://creativecommons.org/licenses/by-nc-nd/4.0/>). <https://doi.org/10.1063/5.0221943>

I. INTRODUCTION

The total electron emission yield (TEEY) is a well-known phenomenon of electron–solid interaction where primary incident electrons hitting a surface induce the emission of electrons: secondary (SEE) and backscattered (BSE) electrons. SEE and BSE have been considered accounting for the parasitic multipactor effect in microwave systems. Multipactor is a resonant electron discharge caused by synchronization of the emitted electrons with the electric field and their uncontrolled multiplication at each impact with the surface.

The physical mechanism behind this effect is an avalanche caused by the electrons emitted: a primary electron impacts the surface and depending on its energy and total electron emission yield (TEEY) of the material, a number of secondary and backscattered electrons will be released from the surface, which may in

terms be accelerated by the reversed radio frequency (RF) fields and impact the surface releasing even more electrons and so on. This detrimental effect takes place in an extremely wide range of devices extending from divertors in tokamaks,¹ to space satellites,² antennas,³ power couplers,⁴ and superconducting radio frequency cavities (SRFs)^{5,6} in particle accelerators and can cause consequent energy deposition, leading, for instance, to SRF cavity quenches,⁷ power coupler window breakage, and, in severe cases, vacuum breakdown and the destruction of the RF device. In some particular case, for instance, in SRF cavities, multipacting can originate from a single point, in which case the secondary electrons come back to the emission location, or multiple points that occur in two points symmetric to the equator region.⁸

Consequently, intense research efforts, in all these fields, are pursued to mitigate multipacting and reduce the TEEY of the

surface. Coating the surface with intrinsically low TEEY films such as titanium,⁹ metal nitride,^{10,11} metal carbides,¹¹ chromium oxides,¹² and carbon¹³ was found to be one of the most effective routes to suppress multipacting. Another approach consists of creating periodical surface profiles as an effective way to suppress multipacting by altering electron trajectories.^{14,15}

Coating an RF surface to decrease its TEEY may, however, meet with other necessary design specifications: the thin film resistivity, in particular, can severely affect the RF surface losses. For instance, state-of-the-art superconducting radio frequency (SRF) accelerating cavities used in particle accelerators have reproducible surface resistances of few nano Ohms or quality factors (Q) above 10^{10} .⁶ The presence of non-superconducting, metallic layers within the RF skin depth will increase the surface resistance and decrease Q . In order to mitigate the multipacting effects in SRF cavities, the coating properties requirements are both a low TEEY and an extremely low RF surface dissipation. Other applications such as ceramic windows in an intense RF field and vacuum environments (power couplers, RF wave guides) require on the contrary charge evacuation to prevent charging and arc formations and a low TEEY. The charge evacuation is achieved by finely tuning the thin film resistivity that can be achieved by controlling its thickness and chemical composition.

Another important aspect to take into consideration is the coating uniformity over potentially complex shaped device surfaces, such as particle accelerator accelerating cavities, antennas, periodical surface profiles mentioned previously, or 3D printed embarked structures.

For these particular reasons, we use thermal atomic layer deposition (ALD) as a deposition technique widely known for its excellent uniformity and atomic-level thickness control.^{16,17} ALD is a chemical gas phase synthesis method used in microelectronics,¹⁸ photovoltaics,¹⁹ and battery²⁰ based on cyclic, self-saturating gas surface chemical reactions. It is important to highlight that, unlike other deposition techniques such as evaporation and sputtering where molecules or nanoparticles agglomerate randomly on the surface until they form a continuous film, during an ALD process, the precursor molecules react covalently with the substrate through self-limiting chemical reactions and leave no more than one monolayer of precursor molecules at the surface after each ALD cycle.²¹ The film is, therefore, deposited one monolayer at a time and this stages for an outstanding thickness and chemical composition control and uniformity over other deposition techniques such as chemical vapor deposition (CVD), physical vapor deposition (PVD), and sputtering.

In this paper, we investigate the thickness dependence of the total electron emission yield (TEEY), the chemical composition, and resistivity of titanium nitride nanolayers deposited by thermal ALD and their response to electron bombardment conditioning. The main findings of this study show that for a TiN film of thicknesses above 1.5–2 nm, the maximum TEEY reaches a saturating “bulk” value of 1.85 and 1.25 before and after conditioning, respectively. For comparison, other deposition techniques show a saturation of the max TEEY above a few tens of nanometers on rough ceramic surfaces and highlight the unique film thickness control and uniformity capabilities of ALD as previously measured on Al_2O_3 and MgO films with different thicknesses.²² In addition, the

TABLE I. ALD growth parameters used.

| Parameters | Al_2O_3 | TiN |
|------------------------|----------------------------|---------------------------------|
| Growth temperature | 250 °C | 450 °C |
| Precursors | TMA + H_2O | TiCl_4 + NH_3 |
| Pulse/purges (s) | 1/15 + 1/15 | 2.5/15 + 0.5/15 |
| Number of cycles | 100 | Between 1 and 500 |
| Growth rate (nm/cycle) | 0.094 ± 0.005 | 0.021 ± 0.005 |

sub-nanometer control of the TiN film thickness enables fine-tuning of both the electrical resistivity and the TEEY values of the TiN films. As a proof of concept, the growth process parameters were optimized on coupons to obtain targeted TEEY and resistivity values for SRF cavities application. These parameters were then successfully implemented on a 1.3 GHz niobium cavity used in particle accelerators in our custom-built ALD system. The RF tests conducted at 1.5 K revealed that 1.5 nm of TiN efficiently suppresses multipacting while preserving high quality factors in the 10^{10} .

II. MATERIAL AND METHODS

A. Atomic layer deposition method

The TiN films were deposited on a 9 nm thick film of ALD Al_2O_3 . Both Al_2O_3 and TiN films were deposited *in situ* by thermal ALD in a home-built viscous-flow thermal ALD reactor²³ with a 5 cm diameter and 50 cm long deposition chamber. The reactor temperature was maintained during the deposition process by a computer-monitored resistive heater system in a range of 30–500 °C. Several K-type thermocouples were placed along the length of the flow tubes and the deposition chamber to ensure the temperature. The carrier gas used was ultrahigh-purity nitrogen (UHP, 99.999%) further purified using an inert gas purifier. The flow was maintained constant during the deposition at 250 SCCM with a reactor pressure of 0.9 ± 0.05 mbar. The ALD system is also equipped with a residual gas analyzer (RGA) device to monitor the reactor gas chemical composition and hence following the surface chemical reactions inside the deposition chamber.

The deposition parameters used for the Al_2O_3 ²⁴ and TiN²⁵ coatings are summarized in Table I. The films were deposited on 500 μm thick Si wafer pieces. After the growth, all the TiN/ Al_2O_3 films were cooled down *in situ* to 30 °C prior to air exposure.

The initial 100 cycles of Al_2O_3 were deposited in order to ensure a reproducible growth rate for the TiN films that can be very surface-dependent, in particular, in the nucleation regime of a few cycles.

The ALD on a 1.3 GHz niobium superconducting cavity was carried out in the same ALD reactor, replacing the ALD deposition chamber with the cavity itself (Fig. 1), ensuring a deposition only on the inside of the cavity. Prior to doing the deposition in a Nb cavity, the homogeneity of the film thickness along the cavity profile was measured by x-ray reflectivity (XRR) on Si samples placed along a test 1.3 GHz tesla shape aluminum cavity as shown in Fig. 2.

The ALD deposition test consisted of 100 cycles of Al_2O_3 following the growth parameters listed in Table I. The thickness profile is very homogeneous with an average thickness,

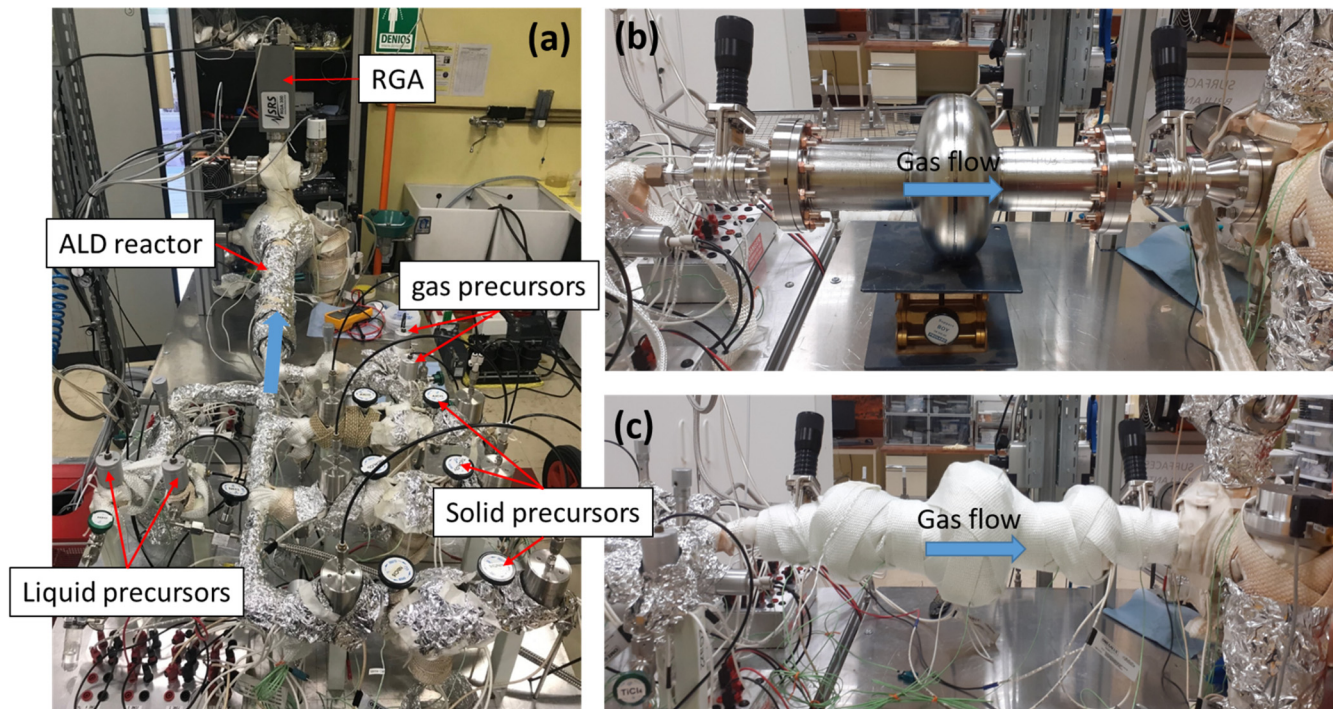


FIG. 1. (a) Top view of the ALD system. (b) A 1.3 GHz cavity is installed on the ALD system, replacing the tube-like ALD reactor chamber. (c) The cavity is dressed with thermocouples, heating resistance, and insulating fiberglass clothes to control its temperature uniformity during the ALD growth. The blue arrows indicate the gas flow direction.

$d = 9.4 \pm 0.5$ nm, and the growth rate per cycle (GPC) is in agreement with literature data.²⁴

B. Electron yield measurements

The TEEY measurements were performed in UHV facility (typically, 1×10^{-10} mbar), specially designed for SEY characterizations.

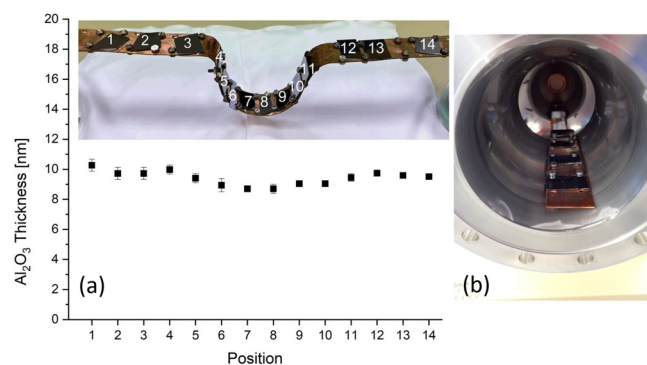


FIG. 2. (a) Thickness profile measured by XRR on Si samples placed on a custom sample holder placed inside a test Al cavity (b).

The analysis chamber is equipped with Kimball Physics ELG-2, Omicron Mg k α /Al k α x-ray source, SIGMA hemispherical electron energy analyzer, Focus FDG150 ion source, and Kimball Physics low energy electron gun ELG2 (1 eV–2 keV).

The TEEY was measured using the protocol described in Ref. 26. In order to avoid additional conditioning of the surface during the TEEY measurement shorts, electron beam pulses of 6 ms and a current of 100 nA were used. Each measurement is repeated and averaged 10 times per point (incident energy) with a typical variation of less than 2%. The incident electron beam was set normal to the surface. The surface conditioning was performed at 500 eV using a high current flood gun Kimball Physics FRA 2X1-2 electron.

C. X-ray photoelectron spectroscopy measurement

The XPS experiments were performed in the same chamber used for the electron yield measurements described previously. The x-ray source is at an incident angle of 60° with respect the sample normal, the emission current was 20 mA, and the working distance between the analyzer and the sample was 30 mm. The analyzer acceptance angle was 20° , and the pass energy filter was set to 20 eV for high resolution scans. These parameters were kept constant for all XPS measurements described in the paper.

The XPS spectra of the Ti 2p and N-1s core-level regions have been analyzed by the peak fitting software CasaXPS²⁷ using a

Shirley-type background and mixed Gaussian/Lorentzian peak shapes. The TiN component of the Ti 2p region was fitted with a line shape extracted from the Ti 2p spectrum of a clean TiN surface deposited by ALD.²⁸

D. X-ray reflectivity

Film thicknesses, roughness, and density were measured by x-ray reflectivity (XRR) using two 5-circle Rigaku Smartlab diffractometers with Cu $K\alpha$ radiation coming from a rotating anode and two different optical setups. The incident beam was parallelized by a parabolic mirror, reducing the angular divergence to approximately 0.01° . Further reduction of the beam divergence was achieved either at the reception part by a parallel slit analyzer (PSA = 0.228°) or at the incidence part by a channel-cut 2-reflection Ge(220) monochromator, which selected also Cu $K\alpha 1$ radiation. 2.5° or 5° Soller slits parallel to the incidence plane were used to limit the transverse divergence of the beam and reduce scattering noise. The reflected beam was counted by a HyPix3000 detector or a NaI scintillation one. The XRR curves were then fitted using X'Pert Reflectivity software to extract the density, thickness, and rugosity of the different layers.

E. Simulations

The secondary emission yield of the electrons has been computed between some eV up to some keV using a Monte Carlo simulation toolkit based on the MICROELEC module of the GEANT4 package.^{29–31} This module has diverse applications, but to address the SEY modeling, some specific physical processes have been accounted for. The quantum reflection/refraction interaction process has been integrated at vacuum/matter or matter/matter interfaces. This code also accounts for the work function (WF) of the material, which influences the behavior of electrons crossing material interfaces. Additionally, at low energies, it is crucial to consider the potential energy of electrons in the material, which becomes significant relative to the incident energy. This involves factoring in the binding energy of each atomic shell and the potential energy of weakly bound electrons in the valence and/or conduction bands. Interaction cross sections are evaluated for each inner shell (K, L, etc.), with a random selection used to determine interactions at each step. Weakly bound electrons in conduction and valence bands are treated similarly, assuming that the excited plasmon systematically dampens by emitting secondary electrons from the band. In this scenario, electrons are presumed to originate from an average energy level representing the band's width. Below some keV, the Monte Carlo code derives interaction cross sections from Optical Energy Loss Functions (OELFs). Mermin's dielectric function provides a description of the momentum transfer. The elastic coulombian interaction cross sections are determined using the ELSEPA code with the partial-wave method. For a deeper understanding of the code, readers can refer to the provided Refs. 29–31.

III. RESULTS AND DISCUSSION

A. Film thickness and growth

The thickness, density, and roughness of the TiN/ Al_2O_3 films were obtained using x-ray reflectivity curves and plotted as a

function of the number of ALD TiN cycles noted N in Fig. 3. For all the samples, the thickness, density, and roughness of the Al_2O_3 films was 9.5 ± 0.06 nm, 3.2 ± 0.2 g/cm³, and 0.4 ± 0.1 nm respectively. We notice two growth regimes depending on the TiN film thicknesses:

For $N > 50$: the film density remains constant and equal to 5.4 g/cm³, which is consistent with the density of bulk-like TiN film found in the literature.³² We observe a linear dependence of the thickness with number of ALD cycles with a growth rate per cycle (GPC) equal to $0.02 \pm 5 \times 10^{-4}$ nm/cycle also in agreement with literature values.²⁵ The film roughnesses are constant around 0.70 – 0.9 nm.

For $N \leq 50$, as the number of cycle decreases, we notice that the density of the films gradually decreases toward the density of TiO_2 that ranges between 3.78 and 4.23 g/cm³ depending on the crystalline phase.³³ This behavior indicates the presence of titanium oxide in the film chemical composition. The growth rate is estimated to be 0.038 ± 0.005 nm/cycles, about twice higher than for the thicker films, which suggests an increased TiCl_4 reactivity on the hydroxyl terminated Al_2O_3 surface as compared to a fully covered TiN surface that occurs around 50 cycles or 2 nm. In this nucleation regime, the TiN film roughness is on the same order as the film thickness.

The secondary electron yield is extremely sensitive to the outermost surface layers properties. It is, therefore, necessary to improve on the TiN film thickness measurement errors obtained by XRR for very thin films ≤ 50 cycles. X-ray photoemission spectroscopy (XPS) was used to not only perform chemical composition analysis of the surface but also to estimate the TiN overlayer average thickness for these very thin films.

The Ti-2p and N-1s XPS spectra are represented in Figs. 4(a) and 4(b) for various TiN film thicknesses from 0 to 100 cycles. The same Shirley background is used to extract the area of Ti 2p

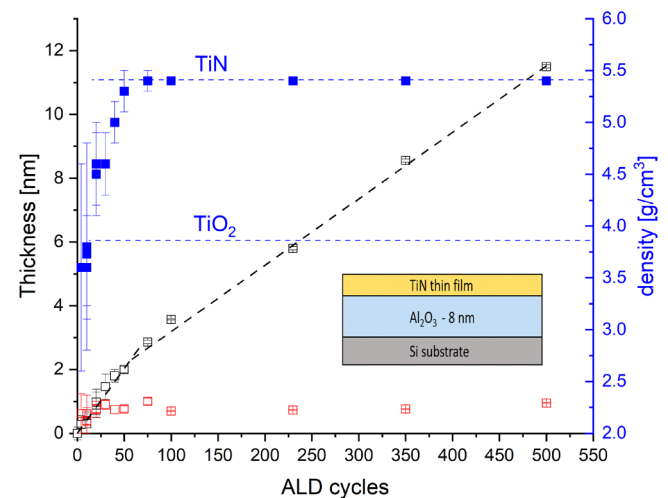


FIG. 3. TiN film thickness (black), roughness (red), and density (blue) extracted from x-ray reflectivity measurements as a function of the number of ALD cycles of TiN.

10 January 2025 14:51:10

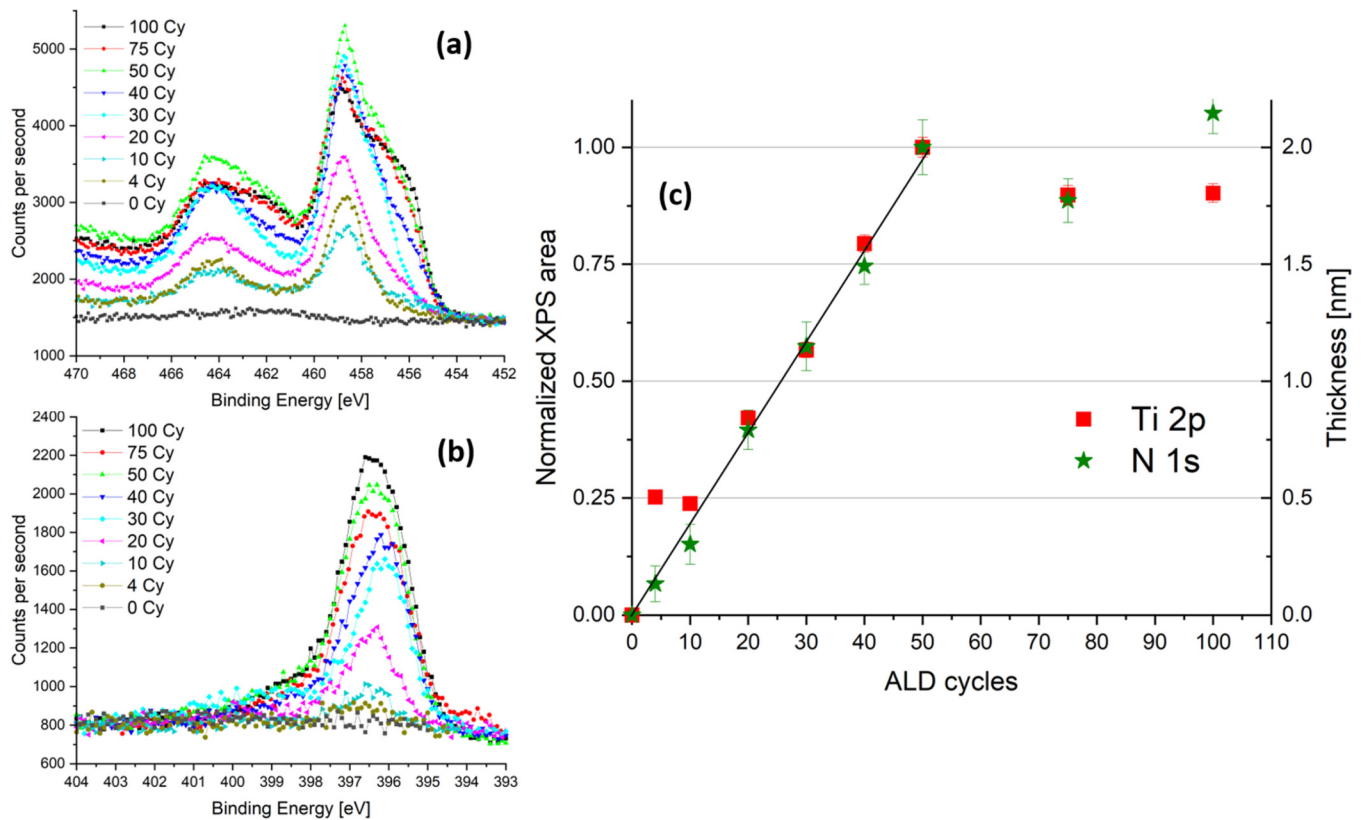


FIG. 4. (a) and (b) represent the Ti-2p and N-1s XPS spectrum measured for different TiN film thicknesses. (c) The area of each spectrum is normalized to the one obtained for 50 cycles of TiN.

emission lines for each spectra that is then normalized by the areas obtained for the 50 Cy TiN film. We can see in Fig. 4(c) that the normalized areas of the core-level Ti-2p and N-1s increase continuously with increasing TiN ALD cycles, until it reaches a saturating value above 50 cycles. This saturation is caused by the finite escape depth of photo-electrons that ranges from a few nanometers for metals to about 10 nm for insulating materials.³⁴ As a result, beyond this threshold the film thickness continues to increase as shown in Fig. 2, whereas the XPS signal intensity saturates.

Based on XRR thickness values obtained for the 50 cycles TiN film and for which the fits give reasonable errors (typically, less than 5% of the TiN film thickness), we can calculate the average thickness of the films <50 cycles with the simple relation: $d_{N \text{ cycles}} = \frac{A_{N \text{ cycles}}}{A_{50 \text{ cycles}}} \times d_{50 \text{ cycles}}$, where $A_{50 \text{ cycles}}$ and $A_{N \text{ cycles}}$ are the area for a 50 cycles and N cycles thick TiN film, $d_{N \text{ cycles}}$ and $d_{50 \text{ cycles}}$ are film thicknesses of the N cycles and the 50 cycles TiN films, which is 2 ± 0.1 nm. The calculated growth rate up to 50 cycles obtained by this method is 0.040 ± 0.002 nm/cycles and the TiN film average thickness errors are a factor of 2 better than the XRR fitting analysis.

The results shown are for as grown films, prior to electron irradiation conditioning. The same procedure was applied after *in situ* conditioning of 400 mC/mm^2 (not shown). We do not

expect the total amount of Ti to be affected by the conditioning, and it was assumed that the total thickness for 50 cycles remains at 2 ± 0.1 nm. Both set of data show very consistent thicknesses before and after conditioning for $N \leq 50$ cycles. For the remaining of this work, the TiN film thicknesses are taken from the XPS analysis for films thinner than 50 cy (or 2 nm) and from the XRR measurements for high number of ALD cycles.

In order to understand the film growth regimes described previously, we propose a simple ALD growth model that calculates the GPC as a function of the number of ALD cycles based on two reaction probabilities of TiCl_4 molecules on the 1/a O-H terminated Al_2O_3 surface, named θ , and 2/ on a surface that reacted with the previous ALD cycle, called θ' . We assume a random distribution of nucleation sites and that the NH_3 pulses do not affect the reaction probabilities mentioned previously. Under those assumptions, we can demonstrate that the TiN growth rate, GR_{TiN} , can be written as a function of the ALD cycle n with the analytical formula

$$\text{GR}_{\text{TiN}}(\theta, \theta', \rho, n) = \rho\theta(1 - \theta)^{n-1} + \rho\theta'(1 - (1 - \theta)^{n-1}), \quad (1)$$

where ρ is a quantum of the average thickness. The left term of the sum describes the growth rate (GR) of the O-H terminated pristine

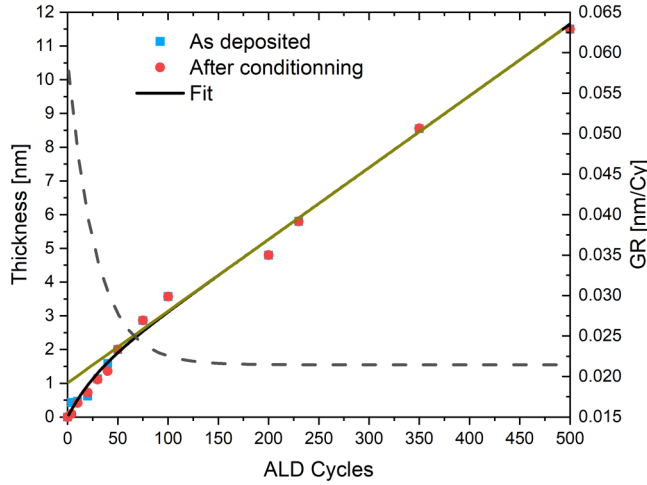


FIG. 5. Measured thickness with XPS and XRR as a function of ALD cycles for as-deposited and conditioned TiN films. The dashed and solid lines are the fits using Eq. (1) for the growth rate GR (right axis) and Eq. (2) for the thickness (left axis).

surface and the right term, the GR on a surface that already reacted with the previous ALD cycle. From Eq. (1), we can calculate the thickness, d , as a function of ALD cycles through the relation

$$d = \int_0^N GR_{\text{TiN}}(\theta, \theta', \rho, n) dn, \quad (2)$$

$$d = \rho\theta'N + \frac{\rho(\theta - \theta')}{(1 - \theta)\ln(1 - \theta)} ((1 - \theta)^N - 1),$$

where N is the total number of ALD cycles. The fit using Eq. (2) shown in Fig. 5 (black curve) gives the values $\rho = 1.6 \pm 0.05$ nm, $\theta = 0.035 \pm 1.10^{-3}$, and $\theta' = 0.013 \pm 5 \times 10^{-4}$. The growth rate can then be calculated as a function of the number of ALD cycles and is represented by the dashed curve in Fig. 5 (right axis). In the limit $N \rightarrow \infty$, formula (1) reduces to the linear dependence represented by the dark yellow line

$$d_{N \rightarrow \infty} = \rho\theta'N - \frac{\rho(\theta - \theta')}{(1 - \theta)\ln(1 - \theta)}. \quad (3)$$

B. The total electron emission yield measurements

The TEEY of the as-deposited bilayer Al_2O_3 -TiN was measured for various TiN film thicknesses. Figures 6(a) and 6(b) show the TEEY measured as a function of primary electron energy from 11 to 1800 eV. All the TEEY curves show a typical shape where the TEEY first increases with the energy of the primary electrons until it reaches a maximum value of TEEY_{MAX} at energy E_{max} and decreases again upon increasing the primary electron energy. Using the measured film thicknesses described in Sec. III A, we can extract the maximum TEEY as a function of TiN film thickness represented in Fig. 7.

Starting from the bare 8.5 nm Al_2O_3 film, the maximum TEEY (TEEY_{MAX}) is 4.65 ± 0.05 at around $E_{\text{max}} = 320$ eV, in agreement with previous literature results with ALD Al_2O_3 .³⁵ As the TiN thickness is increased, the TEEY_{MAX} decreases exponentially to saturating values of 1.87 and 1.25 before and after conditioning for films thicker than ~ 2 nm or 50 ALD cycles (Fig. 7).

Based on the MICROELEC module, a code has been developed to simulate electron transport within a geometry consisting of an 8 nm Al_2O_3 substrate covered by a thin layer of TiN. The thickness of the TiN layer has been varied from 0.2 up to 9 nm. Contamination can also be accounted for, thanks to an additional very thin layer of graphite. The thickness of this layer is defined to be 0.25 nm for the TiN films and 0.1 nm for the bare Al_2O_3 surface. The contaminated surface represents the conditioned sample while the as received sample is supposed to be graphite free. The simulations are summarized in Figs. 6(c) and 6(d). The volume is irradiated with normal incident electrons ranging in energy from 25 eV to 3 keV. All electrons produced during simulation and re-emitted by the surface are counted using a spherical detector surrounding the irradiated volume. Primary and secondary electrons can be distinguished to evaluate secondary emission and elastically backscattered yields. The impact of a change in the TiN layer thickness has been studied and compared to experimental data. TEEY vs incident electron energy has been modeled for the Al_2O_3 substrate topped with TiN thin films of various thicknesses.

The model reproduces well the experimental trends observed; an abrupt decrease of the TEEY max value (Fig. 7) and a gradual shift of TEEY_{MAX} energy toward lower primary electron energies as a function of the TiN film thickness [Figs. 6(c) and 6(d)]. However, it is important to remain cautious with simulations and moderate our conclusions. Statistically, the Monte Carlo method is quite relevant for evaluating energy transfers related to each type of material. On the other hand, when material layers become extremely thin, they lose their uniformity, while the simulation assumes a consistently homogeneous layer. Even though the calculation remains relevant in terms of the probability of interaction with atoms of a given type, we can no longer assert that we have a good understanding of the work function of the material present on the surface nor that we perfectly know the typical excitation energies, such as plasmons, which will be strongly affected by the structure of the surface layer. Nevertheless, considering all these precautions, we find that the simulation is in good agreement with the measurements.

The saturation of the TEEY_{MAX} occurs at ~ 50 ALD cycles (or 2 nm) that corresponds to the change in the TiN growth rate shown in Fig. 5. This observation further supports the nucleation scenario of the TiN film on Al_2O_3 mentioned previously; the partial coverage of the Al_2O_3 surface by TiN up to 50 ALD cycles (or 2 nm) suggests that the TEEY_{MAX} value measured is a combination of Al_2O_3 TEEY_{MAX} and TiN TEEY_{MAX} from 0 to 50 cy. From the dependence of TEEY_{MAX} as a function of the ALD average TiN film thickness and the TEEY_{MAX} values measured on bare Al_2O_3 and bulk TiN, we can extract the TEEY saturation in % as a function of number of TiN ALD cycles N using the formula

$$\text{TEEY saturation (\%)} = \frac{(1 - \text{TEEY}_{\text{MAX}}(N)/\text{TEEY}_{\text{MAX}}(N=0))}{(1 - \text{TEEY}_{\text{MAX}}(N \rightarrow \infty)/\text{TEEY}_{\text{MAX}}(N=0))}. \quad (4)$$

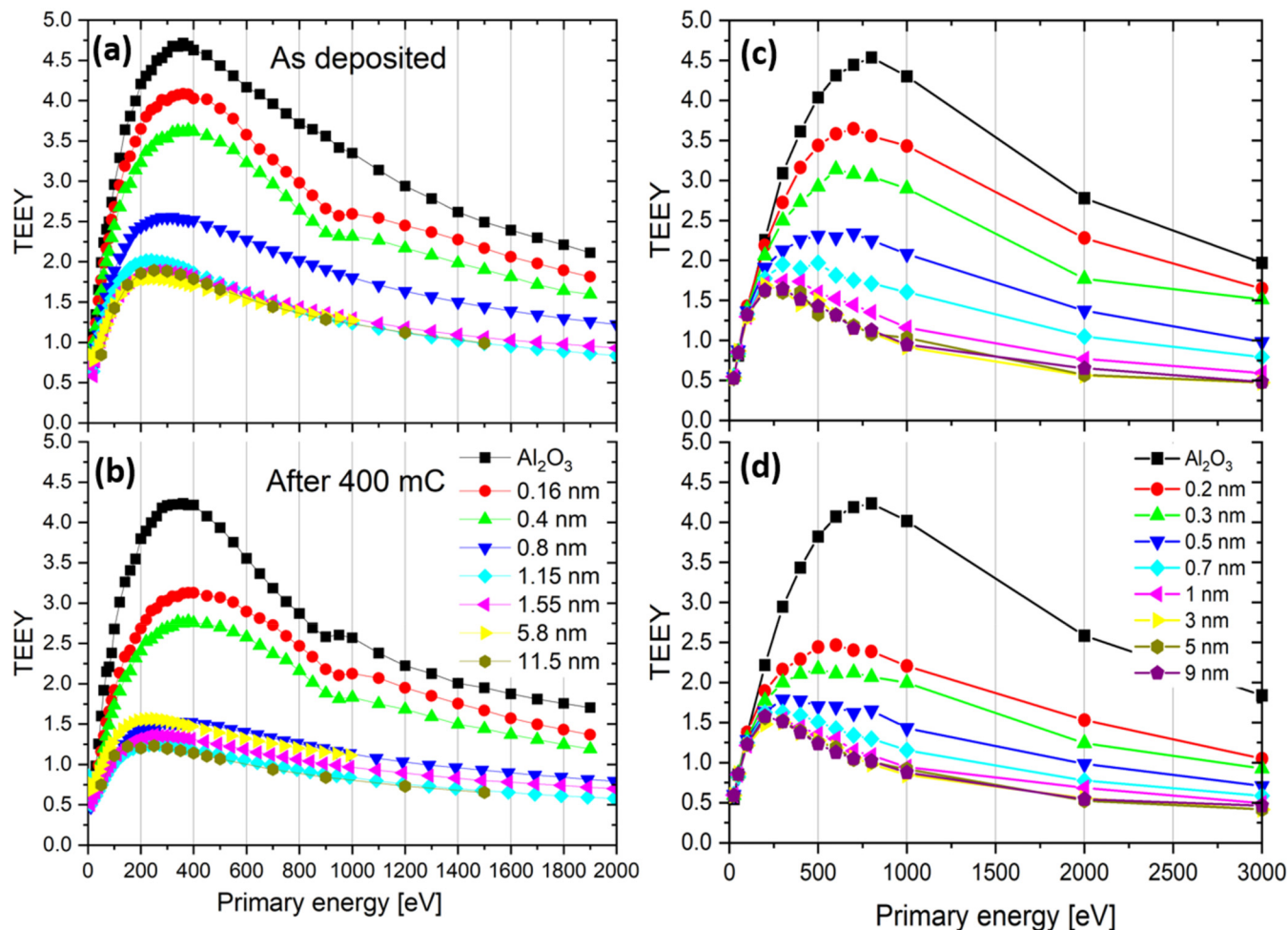


FIG. 6. Experimental data of the TEEY curves before (a) and after (b) 400 mC/mm^2 conditioning for different TiN film thicknesses. (c) and (d) The corresponding numerical simulations using the model described in the text.

The dependence of the TEEY saturation as a function of the TiN average film thickness for the as-deposited and after conditioning is represented in Fig. 8. The TiN surface saturation can be calculated from the ratio: $d/d_{N \rightarrow \infty}$ given by Eqs. (2) and (3) and represented by the black solid line in Fig. 8. The agreement with the data is surprisingly good, considering the simplicity of the nucleation model proposed and proves that the TEEY dependence for very thin TiN films is indeed dominated by the TiN surface saturation in the nucleation regime.

C. Chemical composition analysis and film resistivities

In addition to the TiN film thickness, the TEEY is also sensitive to the surface chemical composition. In order to investigate the thin film's chemical composition and its thickness dependence, XPS measurements were performed *in situ* prior to the

TEEY measurements before and after 400 mC *in situ* conditioning. The Ti chemical composition was extracted from the fits of the Ti 2p peak regions between 454 and 468 eV; three main Ti peaks oxidation states were necessary to correctly fit the data: TiO_2 , TiNO , and TiN , in agreement with previous work.¹¹ The results from the fits of these three oxidation states as a function of the TiN film thickness are displayed in Fig. 9(a). The chemical composition of TiN films shows significant dependence on the layer thickness: for very thin films $\leq 0.5 \text{ nm}$, Ti is essentially in the form of TiO_2 and between 0.75 and 1.7 nm, the film is composed of TiO_2 and TiNO with negligible amount of TiN . As the film thickness increases above 2 nm, all oxidation states tend toward 30%. After *in situ* conditioning with 400 mC [open symbols in Fig. 9(a)], the TiN component of the Ti 2p peak region increases, whereas TiO_2 decreases for film thicknesses above 0.5 nm. This trend can be interpreted as the partial reduction of TiO_2 upon

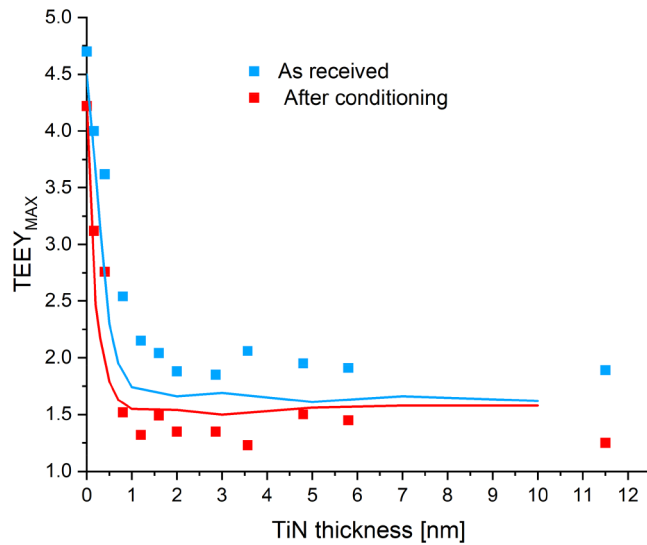


FIG. 7. Maximum value of the TEEY ($TEEY_{MAX}$) as a function of the TiN film thickness before and after conditioning (points), and the values are extracted from the fits displayed in Fig. 6 (lines).

electron surface irradiation as it was observed previously in a number of oxides.^{36,37}

The resistivity of the as-deposited TiN films displayed in Fig. 9(b) was measured with four point probes at room temperature. The bulk resistivity is $63 \mu\Omega \text{ cm}$ and start increasing for film thinner than 10 nm. For films thinner than $\sim 0.8 \text{ nm}$ the resistivity values were too high for our set-up to be measured ($>10^6 \mu\Omega \text{ cm}$).

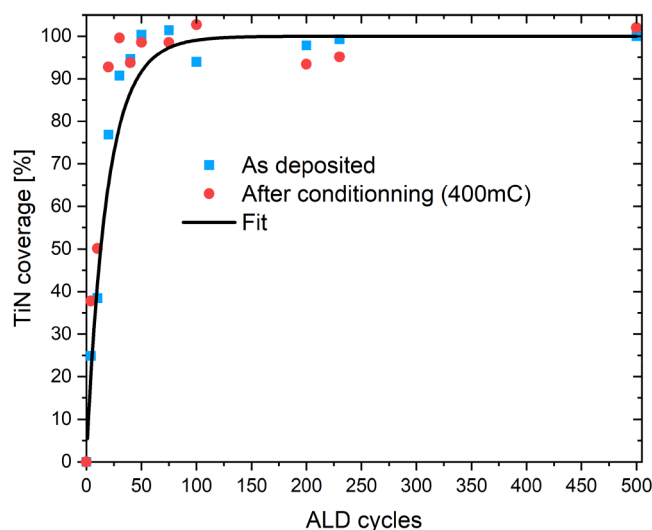


FIG. 8. TiN surface coverage calculated with Eq. (4) before (blue) and after (red) conditioning. The fit (black line) is calculated from the ratio of Eqs. (2) and (3).

Attempts to fit the data with Fuchs³⁸ or Mayadas³⁹ theories that take into account various electron diffusion mechanisms (grain boundaries, point defect, and surface scattering) did not succeed because the experimental resistivity values increase faster than what is predicted by the theory. This can be explained by the change in chemical composition probed by XPS with an increasing insulating TiO_2 component as the film thickness decreases.

IV. RADIO FREQUENCY TESTS ON 1.3 GHz SUPERCONDUCTING NIOBIUM CAVITIES

In order to test the multipacting mitigation approach using a thin TiN layer deposited by ALD, a first attempt was made to deposit 10 nm of Al_2O_3 inside a 1.3 GHz cavity followed by post annealing at 650°C for 10 h in high vacuum (in the 10^{-6} mbar). The purpose of such deposition and annealing procedure is described in Ref. 40 This process was repeated twice on the same cavity with a reset of the surface by chemical etching⁶ in between Al_2O_3 ALD depositions and post annealing. For both RF tests after deposition and post annealing, a strong multipacting barrier reproducibly occurred at 15–18 MV/m and could not be processed, preventing us from reaching higher accelerating fields. Following standard SRF cavity testing procedures, a high pressure rinsing⁴¹ is carried out prior to each RF tests presented in this section.

The baseline RF test measured prior to the ALD deposition (black curve in Fig. 10) reached a maximum E_{ACC} of 32 MV/m with a moderate multipacting barrier present around 21 MV/m and easily processed as expected for Nb cavities.⁴² In order to determine the cause for this strong multipacting barrier, numerical simulations were carried out using Superfish⁴³ and Fishpact⁴⁴ codes to calculate the electromagnetic field distribution and the electron trajectories in a single cell elliptical cavity. The electron energy was calculated at each impact with the surface, and the TEEY curves measured [see Fig. 11(a)] for different surface chemical compositions (bare Nb, $\text{Al}_2\text{O}_3/\text{Nb}$, and $\text{TiN}/\text{Al}_2\text{O}_3/\text{Nb}$) on cavity grade Nb coupons were used to calculate the number of secondary electrons emitted as a function of E_{ACC} in 1.3 GHz geometry. For more details, see Ref. 45.

The numerical simulations [Fig. 11(b)] reveal a maximum of emitted secondary electrons between 16 and 19 MV/m in very good agreement with the experimental data (Fig. 10). In addition, the simulation indicates three orders of magnitude higher electron emission with a $TEEY_{MAX}$ of Al_2O_3 of 4.6 as compared to the bare Nb surface with a $TEEY_{MAX}$ of 2.3. This indicates that the large $TEEY_{MAX}$ value of Al_2O_3 coating is responsible for the observed multipacting barrier. Moreover, it suggests that coating the cavity innerwalls with a 5 nm TiN film deposited on top of a 10 nm thick Al_2O_3 film can reduce the multipacting probability by 6 orders of magnitude compared to that in the Al_2O_3 -coated cavity and, therefore, should suppress the multipacting effect encountered. The number of emitted electrons can even be reduced compared to a bare niobium cavity.

In order to verify the numerical simulations, we deposited two different thicknesses of TiN on previously tested Al_2O_3 -coated and annealed Nb cavities (blue and red curves in Figs. 10 and 12). The RF tests are summarized in Fig. 12. The RF performances after a 5 nm (230 ALD cycles) TiN film coating [green curve in Figs. 12(a) and 12(b)] revealed significantly degraded quality factors (Q) with

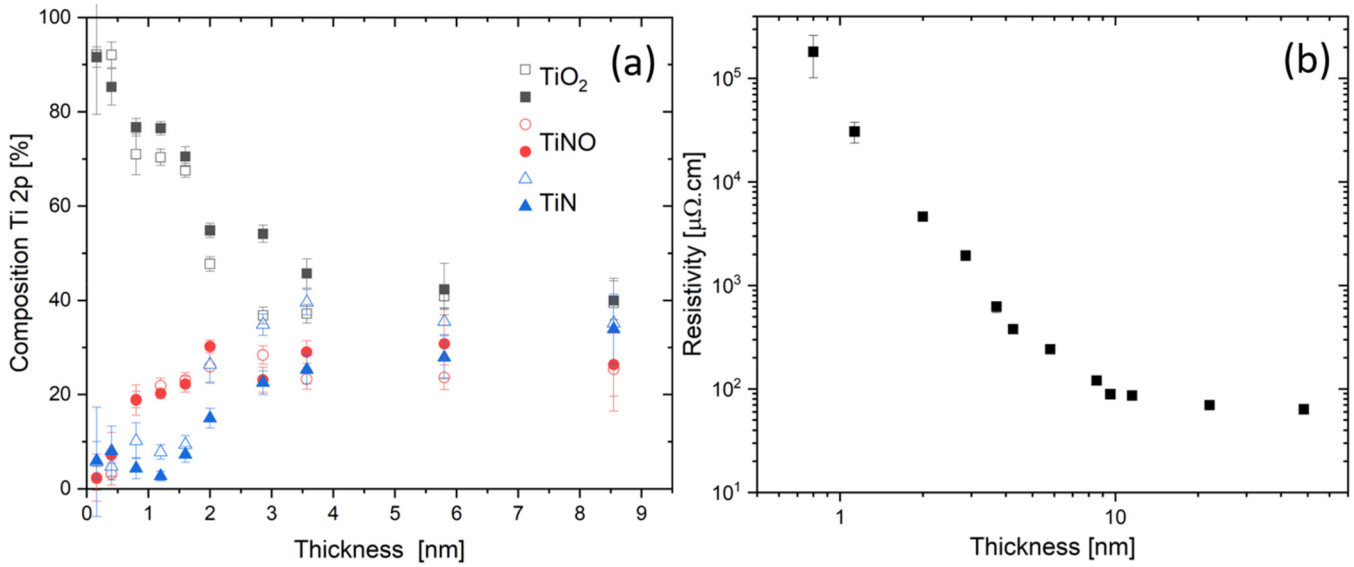


FIG. 9. (a) Composition of the Ti 2p spectrum as a function of the TiN film thickness. Close and open symbols correspond to measurements before and after 400 mC/mm² *in situ* conditioning. (b) Resistivity dependence on the TiN film thickness.

respect to the Al₂O₃-coated cavity baseline; the *Q* values are decreased by over 2 orders of magnitude down to 10⁸ and correspondingly the surface resistance increases 330 times to 2200 nΩ. The measurement errors on the *Q* for such poor values are important (~100%) due to the large mismatch between the power transmission and the cavity. The second RF test was conducted after a

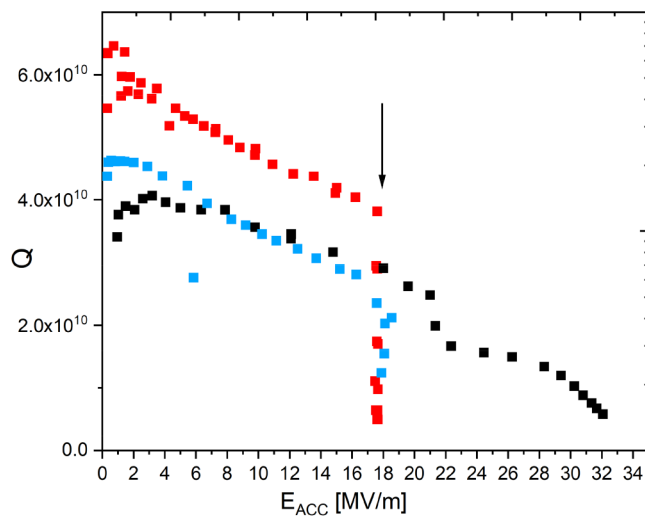


FIG. 10. RF tests of a 1.3 GHz Nb cavity baseline (black points) with two 10 nm Al₂O₃ coatings and post annealing (red and blue points). The multipacting barrier is indicated by the black arrow.

1.6 nm (40 ALD cycles) TiN coating, and the measurements are shown in Figs. 12(c) and 12(d). The quality factor is now in the 10¹⁰ range, 2 orders of magnitude higher than for the previous RF test with a 5 nm TiN coating. Correspondingly, the surface resistance decreases from 2200 down to 10.8 nΩ at low temperatures [Figs. 12(b) and 12(d)] upon reducing the TiN thickness from 5 to 1.6 nm. Importantly, the multipacting barrier at 18 MV/m disappeared, extending the range of accelerating gradient from 18 up to 35 MV/m and recovering the bare Nb RF maximal E_{ACC} performance (black curve in Fig. 10).

The presence of a thin, non-superconducting, metallic layer within the RF penetration depth can affect the dissipation and the surface resistance. Following the calculations of Ref. 46, one can estimate the surface resistance *R_S* of a thin normal film decoupled from the bulk superconductor underneath with the formula

$$R_S = R_{S0} + R_{TiN}, \quad R_{TiN} = \mu_0^2 \omega^2 \lambda^2 \sigma_{TiN} d, \quad (5)$$

where *R_{S0}* and *R_{TiN}* are the bulk superconductor and thin TiN surface impedances; σ_{TiN} , λ are the TiN conductivity and the bilayer penetration depth assumed to be close to the one for Nb (~100 nm). *d* is the TiN film thickness, and ω is the RF pulsation.

The resistivity value [Fig. 9(b)] of a 5 nm TiN film is ~300 μΩ cm, and the numerical estimate gives $R_{TiN} \sim 10^{-7} \Omega$ and $= \frac{G}{R_{TiN}} = \frac{271}{10^{-7}} \sim 10^9$. This value is a bit higher than what is measured with a *Q* of 10⁸ [Fig. 12(a)]. A possible explanation is that the annealing step with TiN coating might have affected slightly the Nb superconductor underneath. For the second coating, the TiN film thickness was decreased down to 40 cy ~1.6 nm that corresponds to the minimal thickness before which the TEEY_{MAX} increases above the bare Nb surface value of ~2.3.

10 January 2025 14:51:10

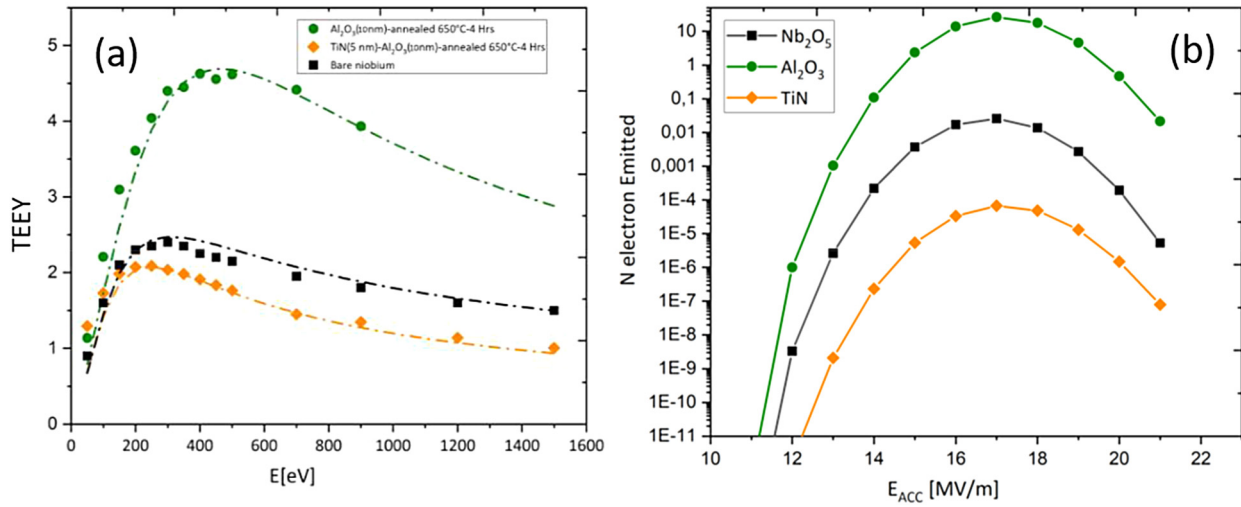


FIG. 11. (a) TEEY curves measured as a function of incident electron energy for the various surface composition indicated. (b) The corresponding numerical simulations of the number of electron emitted into the SRF cavity as a function of accelerating field.

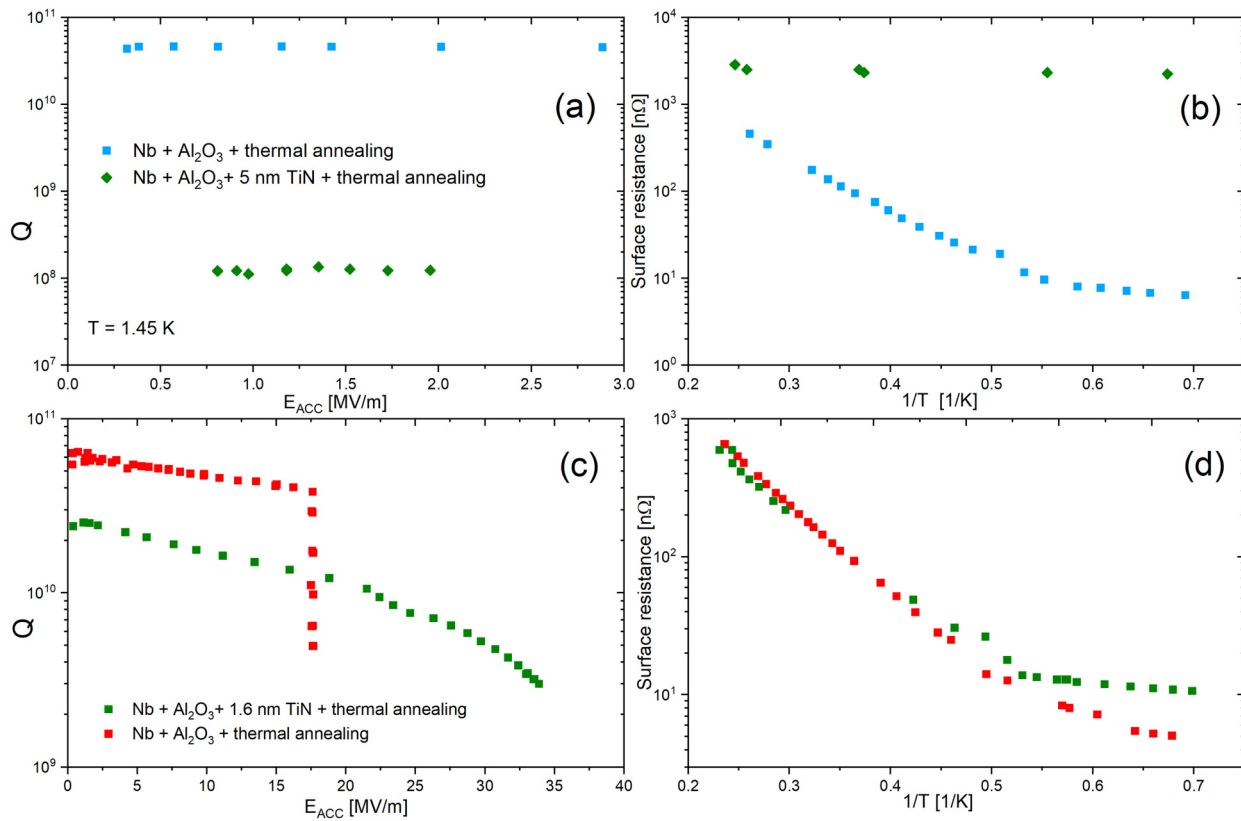


FIG. 12. RF tests at 1.45 K of an ALD coated Nb cavity. The blue and red curves are the RF tests after 10 nm coatings of Al_2O_3 and post-annealed at 650°C in high vacuum, (a) and (b) with an additional 5 nm TiN layer (green curves) and (c) and (d) with a 1.6 nm TiN film (green curves).

10 January 2025 14:51:10

The film resistivity for 1.6 nm increases by about 2 orders of magnitude [Fig. 9(b)] to $\sim 2.10^4 \mu\Omega \text{ cm}$ as compared to the 5 nm thick TiN film. According to Eq. (5), $R_{\text{TiN}}(5 \text{ nm})/R_{\text{TiN}}(1.6 \text{ nm}) = 5/1.6 \times \sigma_{\text{TiN}}(1.6 \text{ nm})/\sigma_{\text{TiN}}(5 \text{ nm}) \sim 100$, so we expect $R_{\text{TiN}}(1.6 \text{ nm})$ to be 100 times smaller than $R_{\text{TiN}}(5 \text{ nm})$ down to $\sim 10^{-9} \Omega$ that is close to what is measured: 5 n Ω above the baseline as shown in Fig. 12(d).

These results demonstrate the ability of ALD to successfully mitigate the multipacting in SRF cavities by tuning both the TEEY_{MAX} and the film resistivity owing to the unique ALD film thickness control capability on complex shape objects.

V. CONCLUSION

In this paper, we have investigated the ALD growth TiN film thickness dependence of the TEEY, chemical composition, and resistivity. The ALD growth mechanisms explained by a simple model lead to an incomplete surface saturation of TiN for films thinner than 1.5–2 nm. Consequently, the TEEY_{MAX} values can be understood as a linear combination of Al_2O_3 and the TiN TEEY_{MAX} respective values. For film thicker than 2 nm, the surface is fully covered with TiN, and the TEEY_{MAX} values saturate. The TiN film resistivities increase exponentially below 10 nm, ranging from $63 \mu\Omega \text{ cm}$ in the bulk limit to over $10^5 \mu\Omega \text{ cm}$ for the 1 nm thick film. The careful selection of a suitable set of TEEY_{MAX} and resistivity values by finely tuning the TiN film thickness enabled the suppression of the multipacting phenomena observed in SRF cavities while maintaining the high quality factor of the superconducting resonators in the 10^{10} range. The results presented here prove that the ALD-based surface engineering is a viable technological route to successfully mitigate multipacting in SRF cavities that could be applied to various cavities shapes. In addition, the scalability of ALD from coupons to the real device is an opportunity to apply this method to other particle accelerator devices such as drift tubes or power couplers, and other RF devices used in satellites for instance with their own optimal resistivities and TEEY values requirements.

ACKNOWLEDGMENTS

The authors would like to thank Thierry Pepin-Donat from IJCLab for providing a HV thermal treatment and Claire Antoine from CEA for insightful discussions. This project has received funding from the region Ile de France Project SESAME AXESRF, Internal CEA internal funds through the Programme Transverse de Competence-Matériaux et procédés, the European Union's Horizon 2020 Research and Innovation programme under Grant Agreement No 101004730 and Grant Agreement No 730871.

AUTHOR DECLARATIONS

Conflict of Interest

The authors declare no conflict of interest.

Author Contributions

Y. Kalboussi: Conceptualization (equal); Data curation (equal); Formal analysis (equal); Investigation (lead); Methodology (equal);

Resources (equal); Validation (equal); Visualization (equal); Writing – original draft (equal). **S. Dadouch:** Investigation (equal). **B. Delatte:** Resources (equal). **F. Miserque:** Investigation (equal). **D. Dragoe:** Investigation (equal). **F. Eozenou:** Resources (equal). **M. Baudrier:** Resources (equal). **S. Tusseau-Nenez:** Investigation (equal); Writing – original draft (equal). **Y. Zheng:** Investigation (equal); Writing – original draft (equal). **L. Maurice:** Resources (equal). **E. Cenni:** Resources (equal). **Q. Bertrand:** Resources (equal). **P. Sahuquet:** Resources (equal). **E. Fayette:** Resources (equal). **G. Jullien:** Resources (equal). **C. Inguibert:** Investigation (equal); Software (equal); Writing – original draft (equal). **M. Belhaj:** Data curation (equal); Investigation (equal); Writing – original draft (equal). **T. Proslie:** Conceptualization (equal); Data curation (equal); Formal analysis (equal); Funding acquisition (lead); Investigation (equal); Methodology (equal); Project administration (lead); Resources (equal); Supervision (lead); Validation (equal); Visualization (equal); Writing – original draft (equal).

DATA AVAILABILITY

The data that support the findings of this study are available from the corresponding authors upon reasonable request.

REFERENCES

- 1J. P. Gunn, "Evidence for strong secondary electron emission in the tokamak scrape-off layer," *Plasma Phys. Controlled Fusion* **54**, 085007 (2012).
- 2A. V. Streltsov, J.-J. Berthelier, A. A. Chernyshov, V. L. Frolov, F. Honary, M. J. Kosch, R. P. McCoy, E. V. Mishin, and M. T. Rietveld, "Past, present and future of active radio frequency experiments in space," *Space Sci. Rev.* **214**, 118 (2018).
- 3J. M. Golio, *The RF and Microwave Handbook* (CRC Press, Boca Raton, FL, 2001).
- 4J. Lorkiewicz, B. Dwersteg, W.-D. Möller, D. Kostin, M. Layalan, and A. Brinkmann, "Anti-multipactor TiN coating of RF power coupler components for TESLA at DESY," Technical report No. CM_P00047838, 2004.
- 5R. Prakash, A. R. Jana, and V. Kumar, "Multipacting studies in elliptical SRF cavities," *Nucl. Instrum. Methods Phys. Res. Sect. A* **867**, 128–138 (2017).
- 6J. Knobloch, W. Hartung, H. Padamsee, and F. Newman, "Multipacting in 1.5-GHz superconducting niobium cavities of the CEBAF shape," in *Proceedings of the 8th Workshop on RF Superconductivity*, Padua, Italy (JACoW, 1997).
- 7D. Proch, and U. Klein, "Multipacting in superconducting RF structures," in *Proceedings of the Conference of Future Possibilities for Electron Accelerators, Charlottesville* (Virginia University, 1979), pp. 34–78.
- 8R. L. Geng, "Multipacting simulations for superconducting cavities and RF coupler waveguides," in *Proceedings of the 2003 Particle Accelerator Conference* (IEEE, 2003), pp. 264–268.
- 9W. Vollenberg, P. Costa Pinto, B. Holliger, A. Sapountzis, and M. Taborelli, "Titanium coating of ceramics for accelerator applications," in *Proceedings of the 6th International Particle Accelerator Conference, Richmond, VA* (JACoW Publishing, 2015), pp. 3148–3150.
- 10A. Variola, W. Kaabi, H. Jenhani, P. Lepercq, G. Keppel, V. Palmieri, and F. Strada, "Titanium nitride coating of RF ceramic windows by reactive DC magnetron sputtering," in *11th European Particle Accelerator Conference (EPAC'08)* (JACoW, 2008), pp. 931–933.
- 11E. L. Garwin, F. K. King, R. E. Kirby, and O. Aita, "Surface properties of metal nitrides and metal carbide films deposited on Nb for radio-frequency superconductivity," *J. Appl. Phys.* **61**, 1145–1154 (1987).
- 12J. Lorkiewicz, B. Dwersteg, W.-D. Möller, D. Kostin, M. Layalan, and A. Brinkmann, *Anti-Multipactor tin Coating of RF Power Coupler Components for Tesla at DESY* (DESY, 2004), p. CM-P00047838.

- ¹³M. Angelucci, A. Novelli, L. Spallino, A. Liedl, R. Larciprete, and R. Cimino, "Minimum thickness of carbon coating for multipacting suppression," *Phys. Rev. Res.* **2**, 032030 (2020).
- ¹⁴C. Chang, Y. S. Liu, J. Verboncoeur, C. H. Chen, L. T. Guo, S. Li, and X. L. Wu, "The effect of periodical wavy profile on suppressing windows multipactors under arbitrary electromagnetic mode," *Appl. Phys. Lett.* **106**, 014102 (2015).
- ¹⁵D. Bajek, S. Wackerow, D. A. Zanin, L. Baudin, K. Bogdanowicz, G.-T. E. Valdivieso, S. Calatroni, B. Di Girolamo, M. Sitko, M. Himmerlich, M. Taborrelli, P. Chiggiato, and A. Abdolvand, "Role of surface microgeometries on electron escape probability and secondary electron yield of metal surfaces," *Sci. Rep.* **10**, 250 (2020).
- ¹⁶R. W. Johnson, A. Hultqvist, and S. F. Bent, "A brief review of atomic layer deposition: From fundamentals to applications," *Mater. Today* **17**, 236–246 (2014).
- ¹⁷M. Leskelä and M. Ritala, "Atomic layer deposition chemistry: Recent developments and future challenges," *Angew. Chem. Int. Ed.* **42**, 5548–5554 (2003).
- ¹⁸C. Wiemer, L. Lamagna, and M. Fanciulli, "Atomic layer deposition of rare-earth-based binary and ternary oxides for microelectronic applications," *Semicond. Sci. Technol.* **27**, 074013 (2012).
- ¹⁹J. A. Van Delft, D. Garcia-Alonso, and W. M. M. Kessels, "Atomic layer deposition for photovoltaics: Applications and prospects for solar cell manufacturing," *Semicond. Sci. Technol.* **27**, 074002 (2012).
- ²⁰X. Meng, X.-Q. Yang, and X. Sun, "Emerging applications of atomic layer deposition for lithium-ion battery studies," *Adv. Mater.* **24**, 3589–3615 (2012). 17.
- ²¹S. M. George, "Atomic layer deposition: An overview," *Chem. Rev.* **110**, 111–131 (2010).
- ²²S. J. Jokela, I. V. Vervovkin, A. V. Zinovev, J. W. Elam, A. U. Mane, Q. Peng, and Z. Insepov, "Secondary electron yield of emissive materials for large-area micro-channel plate detectors: Surface composition and film thickness dependencies," *Phys. Procedia* **37**, 740–747 (2012).
- ²³J. W. Elam, M. D. Groner, and S. M. George, "Viscous flow reactor with quartz crystal microbalance for thin film growth by atomic layer deposition," *Rev. Sci. Instrum.* **73**, 2981–2987 (2002).
- ²⁴M. D. Groner, F. H. Fabreguette, J. W. Elam, and S. M. George, "Low-temperature Al₂O₃ atomic layer deposition," *Chem. Mater.* **16**, 639–645 (2004).
- ²⁵L. Hiltunen, M. Leskelä, M. Mäkelä, L. Niinistö, E. Nykänen, and P. Soininen, *Thin Solid Films* **166**, 149–154 (1988).
- ²⁶T. Gineste, M. Belhaj, G. Teyssedre, and J. Puech, "Investigation of the electron emission properties of silver: From exposed to ambient atmosphere Ag surface to ion-cleaned Ag surface," *Appl. Surf. Sci.* **359**, 398–404 (2015).
- ²⁷N. Fairley, V. Fernandez, M. Richard-Plouet, C. Guillot-Deudon, J. Walton, E. Smith, D. Flahaut, M. Greiner, M. Biesinger, S. Tougaard, D. Morgan, and J. Baltrusaitis, "Systematic and collaborative approach to problem solving using X-ray photoelectron spectroscopy," *Appl. Surf. Sci. Adv.* **5**, 100112 (2021).
- ²⁸D. Jaeger and J. Patscheider, "Single crystalline oxygen-free titanium nitride by XPS," *Surf. Sci. Spectra* **20**, 1–8 (2013).
- ²⁹J. Pierron, C. Inguibert, M. Belhaj, T. Gineste, J. Puech, and M. Raine, "Electron emission yield for low energy electrons: Monte Carlo simulation and experimental comparison for Al, Ag, and Si," *J. Appl. Phys.* **121**, 215107 (2017).
- ³⁰Q. Gibaru, C. Inguibert, P. Caron, M. Raine, D. Lambert, and J. Puech, "Geant4 physics processes for microdosimetry and secondary electron emission simulation: Extension of MicroElec to very low energies and 11 materials (C, Al, Si, Ti, Ni, Cu, Ge, Ag, W, Kapton and SiO₂)," *Nucl. Instrum. Method B* **487**, 66–77 (2021).
- ³¹C. Inguibert, Q. Gibaru, P. Caron, M. Angelucci, L. Spallino, and R. Cimino, "Modelling the impact on the secondary electron yield of carbon layers of various thicknesses on copper substrate," *Nucl. Instrum. Method B* **526**, 1–8 (2022).
- ³²A. Satta, G. Beyer, K. Maex, K. Elers, S. Haukka, and A. Vantomme, *Mater. Res. Soc. Symp. Proc.* **D6.5**, 612 (2000).
- ³³N. D. Johari, Z. M. Rosli, J. M. Juoi, and S. A. Yazid, "Comparison on the TiO₂ crystalline phases deposited via dip and spin coating using green sol-gel route," *J. Mater. Res. Technol.* **8**, 2350–2358 (2019).
- ³⁴J. Zemek, S. Hucek, A. Jablonski, and I. S. Tilinin, "Photoelectron escape depth," *J. Electron Spectrosc. Relat. Phenom.* **76**, 443–447 (1995).
- ³⁵J. Guo, D. Wang, Y. Xu, X. Zhu, K. Wen, G. Miao, W. Cao, J. Si, M. Lu, and H. Guo, "Secondary electron emission characteristics of Al₂O₃ coatings prepared by atomic layer deposition," *AIP Adv.* **9**, 095303 (2019).
- ³⁶O. Dulub, M. Batzilln, S. Solovev, E. Loginova, A. Alchagirov, T. E. Madey, and U. Diebold, "Electron-induced oxygen desorption from the TiO₂(011)–2 × 1 surface leads to self-organized vacancies," *Science* **317**, 1052 (2007).
- ³⁷J.-W. Park, A. J. Pedraza, and W. R. Allen, "Irradiation-induced decomposition of Al₂O₃ during Auger electron spectroscopy analysis," *J. Vac. Sci. Technol. A* **14**, 286–292 (1996).
- ³⁸E. H. Sondheimer, "The mean free path of electrons in metals," *Adv. Phys.* **50**, 499–537 (1952).
- ³⁹A. F. Mayadas and M. Shatzkes, "Electrical-resistivity model for polycrystalline films: The case of arbitrary reflection at external surfaces," *Phys. Rev. B* **1**, 1382–1389 (1970).
- ⁴⁰Y. Kalboussi, B. Delatte, S. Bira, K. Dembele, X. Li, F. Miserque, N. Brun, M. Walls, J. L. Maurice, D. Dragoe, J. Leroy, D. Longuevergne, A. Gentils, S. Jublot-Leclerc, G. Jullien, F. Eozenou, M. Baudrier, L. Maurice, and T. Proslir, "Reducing two-level system dissipations in 3D superconducting niobium resonators by atomic layer deposition and high temperature heat treatment," *Appl. Phys. Lett.* **124**, 134001 (2024).
- ⁴¹K. Saito, H. Miwa, K. Kurosawa, P. Kneisel, S. Noguchi, E. Kako, M. Ono, T. Shishido, and T. Suzuki, "Study of ultra-clean surface for niobium SC cavities," in *Proceedings of the Sixth Workshop on RF Superconductivity* (CEBAF, Newport News, 2003), pp. 1151–1159.
- ⁴²H. Padamsee, "50 years of success for SRF accelerators—A review," *Supercond. Sci. Technol.* **30**, 053003 (2017).
- ⁴³K. Halbach and R. F. Holsinger, *Part. Accel.* **7**(4), 213–222 (1976).
- ⁴⁴E. Donoghue, J. Mammoser, L. Phillips, R. Rimmer, M. Stirbet, H. Wang, and G. Wu, "Studies of electron activities in SNS-type superconducting RF cavities," in *Proceedings of the 12th International Workshop on RF Superconductivity* (New York, 2005), p. 4, <https://www.osti.gov/servlets/purl/850269>.
- ⁴⁵Y. Kalboussi, *Nano hétéro-structures pour l'amélioration des performances de supraconducteurs sous champs intenses*, Thèse de doctorat de l'université Paris-Saclay, 2023.
- ⁴⁶A. Gurevich and T. Kubo, "Surface impedance and optimum surface resistance of a superconductor with an imperfect surface," *Phys. Rev. B* **96**, 184515 (2017).